Chinese Chemical Letters 35 (2024) 108585

Contents lists available at ScienceDirect

Chinese Chemical Letters

journal homepage: www.elsevier.com/locate/cclet

Dynamic tracking of exsolved PdPt alloy/perovskite catalyst for efficient lean methane oxidation

Yanling Yang[a,b,1], Zhenfa Ding[a,1], Huimin Wang[c], Jianhui Li[c], Yanping Zheng[c,d], Hongquan Guo[a], Li Zhang[b], Bing Yang[e], Qingqing Gu[e], Haifeng Xiong[c,d,f,*], Yifei Sun[a,d,*]

[a] College of Energy, Xiamen University, Xiamen 361005, China
[b] School of Environment and Civil Engineering, Dongguan University of Technology, Dongguan 523808, China
[c] Department of Chemistry, College of Chemistry and Chemical Engineering, Xiamen University, Xiamen 361005, China
[d] State Key Laboratory of Physical Chemistry of Solid Surfaces, College of Chemistry and Chemical Engineering, Xiamen University, Xiamen 361005, China
[e] CAS Key Laboratory of Science and Technology on Applied Catalysis, Dalian Institute of Chemical Physics, Chinese Academy of Sciences, Dalian 116023, China
[f] Innovation Laboratory for Sciences and Technologies of Energy Materials of Fujian Province (IKKEM), Xiamen 361102, China

ARTICLE INFO

Article history:
Received 20 April 2023
Revised 8 May 2023
Accepted 17 May 2023
Available online 19 May 2023

Keywords:
Exsolution
PdPt alloy
Operando characterization
Methane conversion
Deep-oxidation

ABSTRACT

Supported Pd based catalysts are considered as the efficient candidates for low-carbon alkane oxidation for their outstanding capability to break C-H bond. Whereas, the irreversible deactivation of Pd based catalysts was still frequently observed. Herein, we reinforced the extruded Pd nanoparticles with quantitive Pt to assemble the evenly distributed PdPt nanoalloy onto ferrite perovskite (PdPt-LCF) matrix with strengthened robustness of metal/oxide support interface. We further co-achieved the enhanced performance, anti-overoxidation as well as resistance of vapor-poisoning in durability measurement. The operando X-ray photoelectron spectroscopy (O-XPS) combined with various morphology characterizations confirms that the accumulation of surface deep-oxidation species of Pd^{4+} is the culprit for fast activity loss in exsolved Pd system, especially at high temperature of 400 °C. Conversely, it could be completely suppressed by *in-situ* alloying Pd with equal amount of Pt, which helps maintain the metastable Pd^{2+}/Pd shell and metallic solid-solution core structure. The density function theory (DFT) calculations further buttress that the dissociation of C–H was facilitated on alloy/perovskite interface which is, on the contrary, resistant toward O–H bond cleavage, as compared to Pd/perovskite. Our work suggests that the modification of exsolved metal/oxide catalytic interface could further enrich the toolkit of heterogeneous catalyst design.

Natural gas fueled vehicles (NGVs) have been maturely developed and widely applied in transportation due to their reduced emission of CO_2 and harmful gasses [1,2]. In NGVs, the catalytic converter is required in exhaust to oxidize the unburned CH_4 since it brings the greenhouse effect 20 times higher than CO_2 [3,4]. However, the completed conversion of lean methane is difficult because of the high energy barrier for dissociative adsorption of methane, which requires the novel catalysts with high activity, thermal stability and water resistance. It is well known that supported palladium catalysts show high activity in methane oxidation [5,6]. Previous experimental and DFT simulation results have confirmed that a surface Pd oxide/bulk metallic Pd catalyst is the reactive phase, which is more active than PdO nanoparticles [7,8]. However, such hybrid architecture is unstable, especially due to the presence of excess oxygen and steam in reactant stream. The former one leads to the generation of inactive PdO_2, and the later one results in the competitive occupancy of OH bonding on Pd (up to 97% on PdO (101) to suppress the absorption of CH_4 [9].

Recently, a novel fabrication principle, exsolution, has showed potential to overcome the drawbacks of poor stability and dispersity of heterogeneous combustion catalysts prepared by conventional impregnation methods [10–12]. The active cations were preliminarily incorporated into the lattice of support oxide, and then extruded out as metallic/alloy nanoparticles attaching on surface, offering the catalytic interface enhanced robustness and reactivity. However, our previous work exemplified the unsatisfied results that the methane oxidation performance of Pd exsolved perovskite

* Corresponding authors.
E-mail addresses: haifengxiong@xmu.edu.cn (H. Xiong), yfsun@xmu.edu.cn (Y. Sun).
[1] These authors contributed equally to this work.

https://doi.org/10.1016/j.cclet.2023.108585
1001-8417/

oxide ($LaFeO_3$) catalyst is poor with T_{50} of 540 °C. Also, it still suffers from severe degradation by 44% in only 30-h stability test presumably due to the irreversible alternation of surface Pd species, and the fundamental reason is still unknown [13].

Many highly performed and degradation resistant Pd-based catalysts have been developed by adding host metallic promotors, such as Pt [14]. The addition of Pt helped to stabilize Pd in a reduced state by forming PdPt alloy that are not readily hydroxylated by vapor [15,16]. Systematical study further unveiled that the stability and performance of alloy catalyst showed composition dependence [15]. Unfortunately, a Pt-additive induced decrease in activity is also widely reported, because Pt prevents the formation of a partially oxidized PdO phase, the acknowledged highly active site for methane combustion [17,18]. These complexed and paradoxical conclusions are linked to fact that different fabrication method can result in a wide range of moieties including Pd, PdO, PdO_2, Pt, PtO_2, alloy, core-shell, mushroom-like, *etc*. [19–22]. Therefore, there is an urgent need to advance Pt decorated Pd site with well-defined nature, and to promote the durability without sacrifice of activity.

In this work, using exsolution approach, we developed the PdPt nanoalloy anchored perovskite ferrite catalyst derivated from a Pt/Pd co-doped $La_{0.9}Ce_{0.1}Fe_{0.97}O_3$ precursor and following N_2 thermal treatment. We showed that the as-prepared PdPt alloy pinned in perovskite is thermally stable and completely reversible from water poisoning, demonstrating enhanced reactivity in methane oxidation in the meantime. The operando X-ray photoelectron spectroscopy (XPS) illustrated that the exsolved PdPt migrated the unexpected formation of surface highly oxidized Pd species (Pd^{4+}), helped maintaining the reactive PdO/Pd hybrid phase for long-term usage. Moreover, the exsolved PdPt alloy/perovskite interface overcomes the drawback of pure Pd system that are readily and irreversibly poisoned by vapor additive. Our work grants a new thinking for the development of novel and stable heterogeneous supported catalyst toward various combustion reactions.

First, we employed sol–gel method to prepare Pd and Pt (co-)doped LCF perovskite precursor in which the Pd or Pt ions were atomic dispersed in the lattice. And then, all perovskites were pretreated by N_2 atmosphere to trigger the exsolution of Pd, Pt and PdPt alloys, respectively. The crystallinity of all materials was systematically characterized by XRD patterns (Fig. 1a). All precursors including LCF, LCFPd, LCFPt and LCFPdPt show clear diffraction peaks at ~22.7°, 32.3°, 39.8°, 46.3°, 52.0°, 57.5°, 67.5° and 76.7°, which are ascribed to the (101), (121), (220), (202), (141), (240), (242) and (204) planes of $LaFeO_3$ parent perovskite (PDF#37–1943), respectively [23]. The location of 100% intensity diffraction peak of (121) plane was selected as the standard to study the influence of heteroatom doping and exsolution on unit cell parameter of the materials. The incorporation of Pd, Pt and Pd-Pt shifts the location of XRD peak from 32.29° to 32.22°, 32.22° and 32.17°, respectively (Fig. S1 in Supporting information). And such red shift is correlated to the increase of lattice volume, owing to the substitution of larger Pd and Pt with smaller Fe in BO_6 octahedron. The ion radiuses for Pd^{4+}, Pt^{4+} and Fe^{3+} are 0.62 Å, 0.63 Å and 0.49 Å, respectively [24]. The diffraction peaks ascribed to perovskite of all materials maintain well after the exsolution of corresponding dopants (thermal N_2 treatment). Nevertheless, the blue shift of diffraction peak to higher angle could be observed (Fig. 1b), signifies that certain amount of Pd^{4+} and Pt^{4+} species migrated from the host lattice to the surface, leading to the shrinkage of unit cell. H_2-TPR experiments were conducted to understand the reducibility of the catalysts (Fig. 1c). The reduction property of doped samples is apparently distinct from the impregnated analogues (Fig. S2 in Supporting information). More importantly, the additive of Pt alters the reduction thermodynamic of Pd, and the H_2 consumption at 207 °C, 62 °C and 78 °C for LCFPt, LCFPd and LCFPdPt samples are assigned to the reduction of Pt^{4+}, Pd^{4+} and Pd^{4+}-Pt^{4+}, respectively [25–27]. For comparison, the Pd-LCF, Pt-LCF and PdPt-LCF catalysts after exsolution were further measured by H_2-TPR (lower plot in Fig. 1c). The hydrogen release from Pd-LCF (negative peak at about 64 °C), attributes to the decomposition of Pd β-hydrides, evidencing the existence of surface metallic Pd [28]. The absence of β-hydrides peak on Pt-LCF and PdPt-LCF suggests the prohibited formation of hydrides which only happen on metallic palladium [14]. This result proves the exsolved PdPt alloy, rather than isolated Pt/Pd as predominant species on PdPt-LCF. The surface enrichment of Pt and Pd elements migrating from bulk is further quantitively buttressed by the results of summarized XPS data (Fig. 1d). The ratio of Pd/(La+Ce) for LCFPd and LCFPdPt is 7.58% and 4.5%, respectively, which then increases to 10.5% and 11.8% after exsolution. Meanwhile, the ratio of Pt/(La+Ce) raises from 3.6% to 5.9% for LCFPdPt after exsolution. The surged surface concentration of Pd and Pt agrees with our speculation regarding exsolution of Pd and Pt.

The TEM characterization was used to deeply analyze the morphology of exsolved alloy, perovskite matrix as well as their interface. As shown in Fig. S3 (Supporting information), the FFT pattern of selected region of LCFPdPt provides the evidence for the perovskite phase. Moreover, the Ce, Pd and Pt are uniformly dispersed, as shown in high-angle annular dark-field scanning TEM (HADDF-STEM) and EDX elemental mapping images. After N_2 treatment, the exsolved nanoparticle pinned into the perovskite can be clearly observed (Fig. 1e), as marked in right dashed yellow frame. It possesses the interplanar spacings of 0.201, 0.225 and 0.141 nm derived from the responding diffraction spots in FFT pattern image, which can be felicitously assigned to PdPt (220), (111) and (200) planes, respectively. The left dashed frame points to the lattice fringe of $LaFeO_3$ perovskite. The AC HADDF-STEM image shown in Fig. 1f clearly illustrated the lattice distance of 0.132 nm which can be ascribed to the (220) plane of PdPt alloy. The particle size is around 7 nm. Fig. 1g is the HAADF STEM image corresponding EDX elemental mapping images of another suspected PdPt alloy nanoparticle. Clearly, the Pt signal matched well with Pd in the bright spot region with negligible variation in element distribution of La, Ce, Fe and O, which can be a powerful evidence supporting the formation of PdPt alloy. It is worthy noticed that, the co-exsolution of Pt and Pd from perovskite is a highly selective way to trigger generation of alloy in our study. This conclusion is supported by the TEM data (Fig. S4 in Supporting information) of impregnated Pt on exsolved Pd-LCF catalyst in which Pt and Pd species exist as isolated nanoparticles without forming solid solution.

We further systematically study the exsolution behavior of catalyst with different Pd/Pt ratios. Fig. S5 (Supporting information) demonstrates the XRD patterns of catalysts with Pd/Pt ratio of 2 and 0.5 in precursor and exsolved moiety, respectively. There is still no diffraction peak related to isolated Pd and Pt species, even the Pt+Pd level reach 9% in total. As expected, the exsolved particles with the average size of are 3.1 nm and 7.7 nm could be distinguished on $PdPt_2$-LCF, and Pd_2Pt-LCF, respectively (Figs. S6 and S7 in Supporting information). Furthermore, the line scanning results prove that the exsol-ved particles are all belong to the PdPt solid solution but with concentration variation, as demonstrated by the gradually enhanced intensity of Pt signals with the increasing Pt content. Therefore, it can be concluded that the addition amount of Pt can regulate the surface composition of exsolved alloy.

When the perovskite precursors treated with N_2, the driving force for exsolution of PdPt alloys originates from the low partial pressure of oxygen in the N_2 atmosphere which leads to the migration of O^{2-} from the perovskite oxide into gaseous phase in the form of O_2, and simultaneously accompanied with the exsolution

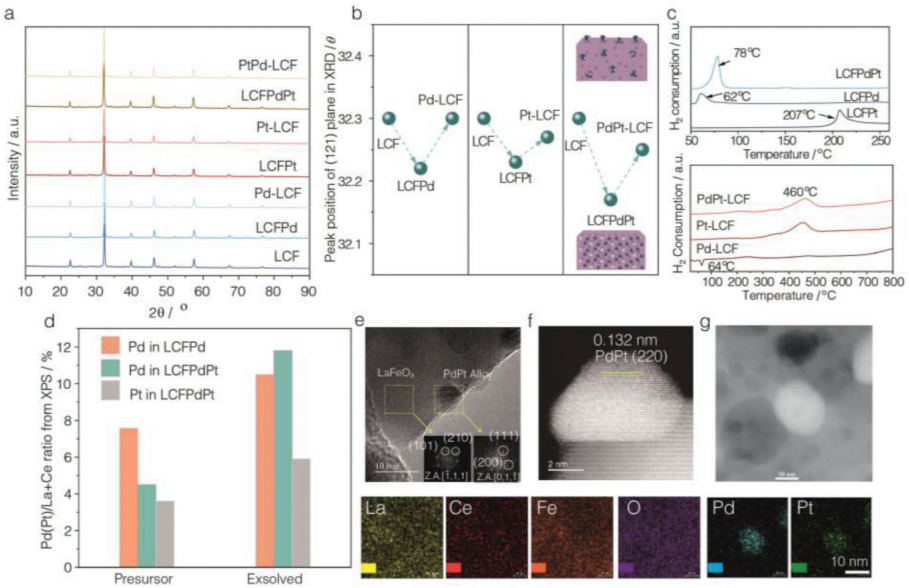

Fig. 1. (a) The XRD patterns of Pt and Pd (co-)doped LCF samples before and after N_2 treatment. (b) The variation trend of the XRD main peak position of catalyst after N_2 treatment in the range from 30° to 35°. (c) The H_2-TPR profiles of LCFPt, LCFPd, LCFPdPt samples before and after N_2 treatment. (d) The Pd(Pt)/(La+Ce) ratio of Pd and Pt based catalysts before and after exsolution according to the XPS spectra. (e) The HRTEM images of PdPt-LCF catalyst and FFT patterns of selected region. (f) AC HADDF-STEM images of an individual PdPt nanoparticle. (g) HADDF-STEM images and EDX elemental map of La, Ce, Fe, O, Pd and Pt for PdPt-LCF.

of PdPt alloy particles to balance the charge neutrality. Therefore, it is reasonable to quantify the amount of exsolved metallic ions based on the amount of oxygen ion released following the equation (Eq. 1) below:

$$LaCeFe_{1-x}(PdPt)_xO_3 \rightarrow LaCeFeO_{3-y} + xPdPt + y/2\ O_2 \quad (1)$$

Following this line of thinking, the mass spectrum (MS) was used to detected O_2 signals generated upon the temperature programmed nitrogen treatment and the results are shown in Fig. S8 (Supporting information). The integrated area of O_2 signal was normalized to the value of 10 mg PdO standard material, to determine the quantity of exsolve ions. Similar as PdO, all perovskite precursors demonstrate remarkable oxygen release signal at ~800 °C, which can be considered as the indicator of exsolution. The ~57% of Pt/Pd cations are calculated to exsolve out from lattice in PdPt-LCF. As the incorporation of more Pt dopants, larger amount of released O_2 is detected, which corresponds to larger amount of exsolve ions (69% for $PdPt_2$-LCF). The thermodynamic of facilitated exsolution of alloy is also confirmed by DFT calculation (Fig. S9 in Supporting information). The calculated formation energies of Pd+O vacancies in LCFPd and Pt+O vacancies in LCFPt is 1.57 and 1.01 eV, respectively. The sum of these two values (2.58 eV) is larger than that of Pd+Pt+2O vacancies in LCFPdPt (2.44 eV).

The catalytic activity under lean methane conditions in region of 200–850 °C was measured on all catalysts. The Pd containing perovskite precursors including LCFPd, LCFPdPt show poor catalytic activity with the T_{50}s (the temperature corresponding to 50% conversion of CH_4) of 530–540 °C which is almost identical to the values of Pt incorporated and impregnated catalysts (Figs. S10 and S11 in Supporting information). These results suggest that the embedded Pd species are inactive toward methane oxidation even with surface decoration of Pt moiety. Fig. 2a displays the light-off curves in CH_4 combustion of Pd-LCF, PdPt-LCF and Pt/Pd-LCF catalysts which all possesses exposed Pd species. The single Pd-LCF exhibits a T_{50} of ~370 °C, and the alloying of exsolved Pd with Pt further lowers the T_{50} to ~335 °C. Such promotion effect is absence on Pt/Pd-LCF with an even higher T_{50} of 375 °C, suggesting the important role of modality of nanoalloy. The stability tests of Pd-LCF and PdPt-LCF catalysts in methane combustion were carried out at an intermediate temperature zone of 350 °C (low conversion rate). There was no obvious deactivation of the two catalysts during the initial 50-h test. Whereas, when the temperature of steady measurement raised to 400 °C (high conversion rate), the CH_4 conversion rate of Pd-LCF sharply declined from 56.8% to 38.3% after 50 h reaction (Fig. 2b). On the other hand, the PdPt-LCF showed a negligible deactivation (variation of ~0.2% in 50 h) at the same temperature and similar initial CH_4 conversion, which means alloyed Pt can promote the stability of exsolved Pd particles at higher CH_4 conversion rate. However, the impregnated of Pt cannot enhance the stability of Pt/Pd-LCF (Fig. S12 in Supporting information), where the CH_4 conversion decreased from 59.9% to 39.8% during 50 h testing. The morphology of exsolve alloy after stability test was further characterized by STEM and EDX analysis (Fig. S13 in Supporting information).

The average particle size of exsolved alloy did not show much change with uniformly dispersed Pt and Pd, as proven by EDX elemental mapping. To test the catalyst activity and stability in humid reactant, methane oxidation was carried out with the addition of vapor (Fig. 2c). Compared to dry gas, the humid reactant leads to a relatively lower activity with T_{50} of ~400 °C on PdPt-LCF (Fig. S14 in Supporting information), probably due to the OH bonding-induced block of reactive sites. However, it still can reach a high conversion of 95% at 500 °C, much superior to 82% of Pd-LCF at same condition. The stability test was first performed for 20 h in 3 vol% steam containing feed and then switch to dry gas for another 20-h (350 °C). The Pd-LCF suffers from severe deactivation (1.3% per hour from point A to B) in humid gas. After two-round measurement up to 80 h, the activity in dry feed has dropped down from 28.5% (point B) to 22.8% (point E). Whereas, PdPt-LCF catalyst demonstrates a much subtle loss of reactivity (0.05% per hour from point A to B) when switching between dry and steam containing methane feeds. And the activity can be fully recovered after 80-h (point E).

To further track the evolution of chemical states of exsolved catalyst under reaction condition, the operando X-ray photoemission spectroscopy (O-XPS) measurements were performed on Pd-LCF and PdPt-LCF. The preprocessing was conducted in *in-situ* cell

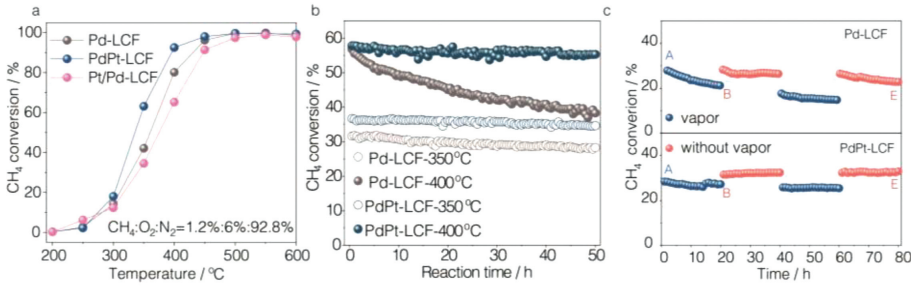

Fig. 2. (a) The catalytic activity of N_2 treated Pd and Pt based catalysts for methane oxidation in dry conditions. (1.2 vol% CH_4, 6 vol% O_2 in N_2, GHSV = 30 000 h^{-1}) of all samples. (b) The methane conversion with the on-stream time in dry experiments at different reaction temperature. (c) Catalyst stability with and without vapor of Pd-LCF and PdPt-LCF catalysts at 350 °C with time on stream.

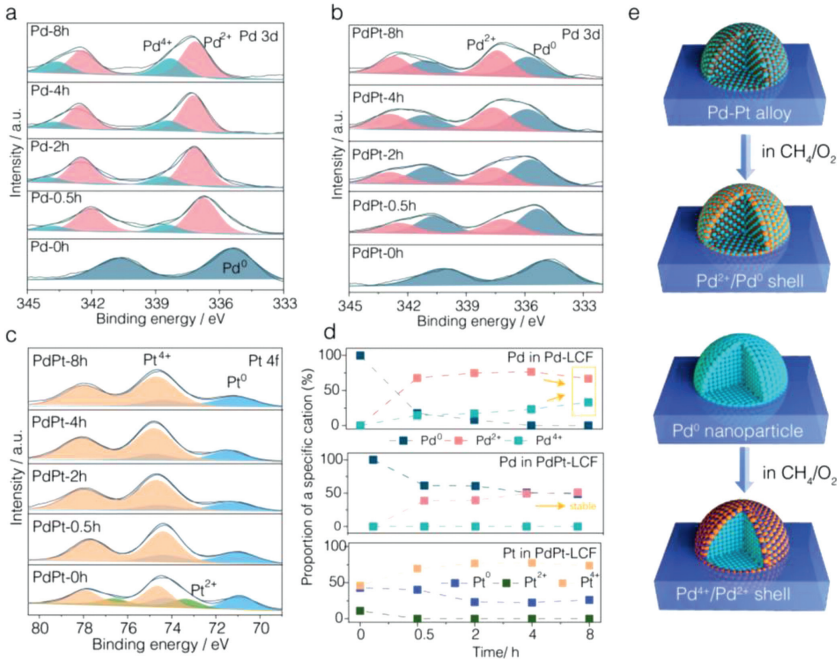

Fig. 3. (a–c) The operando XPS spectra of Pd and Pt in Pd-LCF and PdPt-LCF catalysts treated in 1.2% CH_4/6% O_2/N_2 at 400 °C for 0, 0.5, 2, 4 and 8 h. (d) The responding proportion evolution of Pd^0, Pd^{2+}, Pd^{4+} according to the fitting curve of operando XPS spectra. (e) The schematic of the evolution of exsolved PdPt alloys and Pd particles during methane oxidation. Color scheme: Pd^0, green; Pt^0, dark brown; Pd^{2+}, yellow; Pd^{4+}, purple.

that is connected to the vacuum chamber with a coupling lever and shutter between them. The treatment is preliminarily performed at 400 °C and CH_4 (1.2 vol%)/O_2 (6 vol%)/N_2 (92.8 vol%) atmosphere (1 bar) for various durations (0–8 h). After that, the cell was directly vacuumed without opening, and the sample was transferred into XPS main chamber for measurement. The spectra of Pd 3d and Pt 4f on both samples are shown in Figs. 3a–c, and the Ce 3d and Fe 2p spectra are shown in Fig. S15 (Supporting information). Both Ce and Fe demonstrate no variation during measurement. The summary of the proportion of Pd and Pt with different valences based on the deconvolution of XPS data is shown in Fig. 3d.

We first did the deconvolution for each spectrum and then assigned the corresponding binding energy peaks. For Pd $3d_{5/2}$ spectra, the peaks at 338.3, 336.9 and 335.3 eV could be ascribed to Pd^{4+}, Pd^{2+} and Pd^0, respectively [29,30]. For Pt 4f, the peaks at 71.4, 73.3 and 74.7 eV are assigned to Pt^0, Pt^{2+} and Pt^{4+}, respectively [31]. For PdPt-LCF sample, the initial composition is 42% (Pt^0), 11% (Pt^{2+}) and 47% (Pt^{4+}). After 4-h treatment, more than 75% Pt species is Pt^{4+}which exists in the form of PtO_2. And no Pt^{2+} but certain amount (~25%) of metallic Pt could be detected. While the valence distribution of Pd species of PdPt-LCF is distinct from that of Pd-LCF, and equal amount of Pd^0 and Pd^{2+} was found after 4-h treatment, suggesting the hybrid Pd/PdO phase in PdPt-LCF, which is defined as the reactive site for methane oxidation [32]. Also, such metastable structure is very stable after extended 4-h treatment. In contrast, the pure exsolved Pd system obtain the mixture of Pd^{4+} (25%) and Pd^0 (75%) at the timepoint of 4-h. And the percentage of Pd^{4+} keeps surging to ~35% for another 4-h treatment (yellow dashed rectangular in Fig. 3d), in consistent with its continuously decreased performance. Thereby, the absence of Pd^{4+} in PdPt-LCF could account for high stability, and the exsolution of PdPt alloy could prevent the deep oxidation of Pd species. Above results unambiguously demonstrated that the CH_4 combustion activity is directly related to the stability of PdO (namely, the strength of the Pd-O bond), as well as the chemical state of Pd species. The addition of Pt can reinforce the Pd-O bond thus retard its deep-oxidation. Thereby, combining O- XPS and STEM analysis, we can make the following speculation of the emergence of PdPt alloy (trace amount of oxidized Pt) on perovskite in the initial state. And during operation, the superficial surface of alloy was transformed and stabilized as hybrid of PdO on PdPt-LCF, forming a PdPt/PdO core-shell structure that can co-achieve the good compromise between activity and stability. Conversely, the surface of

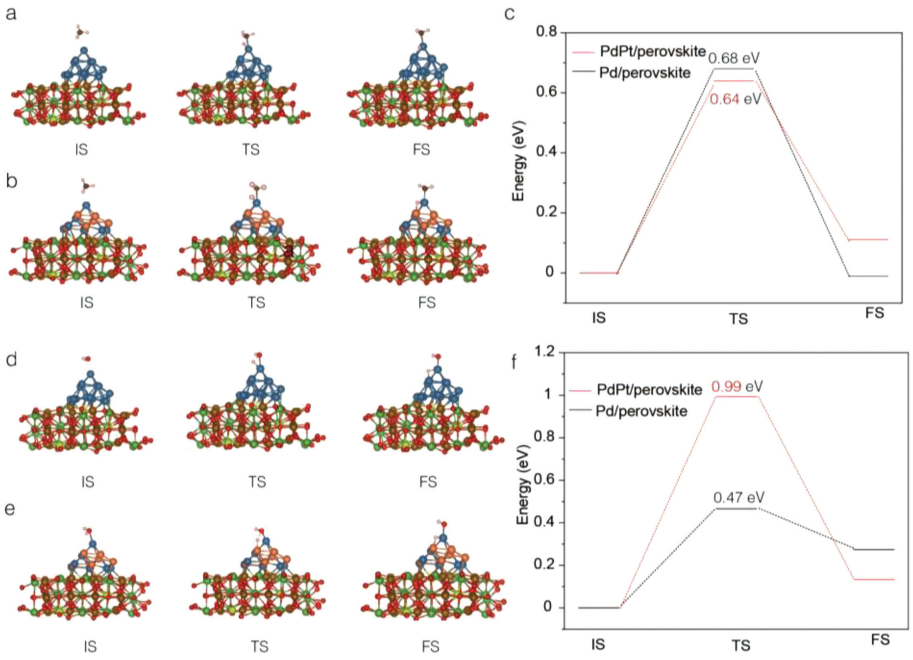

Fig. 4. DFT simulations of methane oxidation and water dissociation over Pd/perovskite and PdPt/perovskite interface. (a, b) Structures evolution during methane oxidation (the initial state (IS), transition state (TS) and final state (FS)). (c) energy barriers of methane dissociation over the Pd/perovskite and PdPt/perovskite. (d, e) Structures evolution during water dissociation (IS, TS and FS). (f) Energy barriers of water dissociation over the Pd/perovskite and PdPt/perovskite. blue presents Pd; orange presents Pt; red presents O; pink presents H; dark brown present C; light brown presents Fe; green presents La; lucifer yellow presents Ce.

exsolved Pd is completed transferred into less-active PdO_2, leading to irreversible and fast performance degradation (Fig. 3e).

Based on the performance measurement and characterizations of physical property of the catalysts, we concluded that the high methane oxidation activity and stability in associated with the exsolved PdPt alloy anchored on perovskite matrix. To further validate the experimental results, we conducted DFT calculations. For these models, the energy barrier for breaking the C–H bond of CH_4 was calculated which is well acknowledged as the rate-determining step for methane oxidation [16]. The models of initial state, transition state and final state are shown in Figs. 4a and b. As shown in Fig. 4c, the activation barrier of methane on Pd (110) perovskite heterostructure is 0.68 eV. In comparison, a lower activation barrier (0.64 eV) for the methane dissociation could be observed on an exsolved alloy/perovskite interface. On the other hand, the enhanced stability in humid feed can also be explained on the basis of DFT calculation results on the dissociation barrier of water molecule on the catalyst (models shown in Figs. 4d and e). Generally speaking, while exposed to humid feed, the generation of Pd hydroxyl species ($Pd(OH)_2$) is the catalytically inactive phase for methane oxidation. Our DFT calculation results show that the dissociation of water molecule to the chemisorbed H^* and OH^* species has an energy barrier of 0.47 eV on Pd/perovskite (Fig. 4f). While on PdPt/perovskite, the barriers for the O–H bond cleavage of water molecule is as high as 0.99 eV, indicating that the alloying effect can inhibit the formation of isolated Pd–OH. Therefore, when exposed to steam, the exsolved PdPt are resistant to H_2O poisoning.

In summary, we have developed a modified exsolution method to synthesize the PdPt alloy anchored perovskite catalytic platform derivated from a Pd/Pt co-doped perovskite precursor. The careful morphology characterization results haveconfirmed that both Pd and Pt metals are intimately mixed in exsolved alloy nanoparticle pinned onto the surface of perovskite with well-defined interface. The exsolved alloy system with an optimal Pd/Pt ratio of 1:1 (PdPt-LCF) demonstrates an outstanding methane oxidation activity with T_{50} of 335 °C, which is apparently superior to the exsolved monometallic Pd system (Pd-LCF) and impregnated Pt modified system. Further stability test stresses that the exsolved alloy system shows no detectable deactivation at conversion rate of 58% for 50 h, while the exsolved Pd catalyst demonstrates a fast deactivation with the declined conversion rate from 56.8% to 38.3%. While exposed to humid feed, the Pd-LCF suffers from a severe deactivation rate of 1.3% per hour which is 25 times faster than that of the water-tolerant PdPt-LCF catalyst (0.05% per hour). We further employed the operando XPS characterizations to both catalytic platforms to illustrate the fundamental reason for their distinct durability. It was found that the exsolved PdPt was transferred into the active Pd^{2+}-Pd^0/PdPt core-shell structure during operation. Whereas, the surface of exsolved Pd were continuously deeply oxidized to form inert Pd^{4+} shell, leading to decreased performance. Our experimental observations are in consistent with the DFT calculation results which show distinctive energy barriers of methane and water dissociations on PdPt alloy/perovskite and Pd/perovskite interfaces, respectively. This work suggests that such approach can be used to modify other supported catalysts toward various heterogeneous catalysis reactions.

Acknowledgments

This work was supported by the National Natural Science Foundation of China (Nos. 22272136, 22202041, 22102135, 22202163, 22172129). Y. Sun acknowledges the Fundamental Research Funds for the Central Universities (No. 20720220119), and Science and Technology Project of Fujian Province (No. 2022L3077). L. Zhang thanks the financial support from Guangdong Basic and Applied Basic Research Fund (No. 2022A1515110239). H. Xiong acknowledges the funds from Science and Technology Projects of Innovation Laboratory for Sciences and Technologies of Energy Materials of Fujian Province (IKKEM) (No. HRTP-[2022]-3) and the Fundamental Research Funds for the Central Universities (No. 20720220008).

References

[1] J.R. Camuzeaux, R.N.A. Alvarez, S.A. Brooks, et al., Environ. Sci. Technol. 49 (2015) 6402–6410.
[2] J. Yang, Y. Guo, Chin. Chem. Lett. 29 (2018) 252–260.
[3] X. Feng, L. Jiang, D. Li, et al., J. Energy Chem. 75 (2022) 173–215.
[4] E. Hong, C. Kim, D.H. Lim, et al., Appl. Catal. B 232 (2018) 544–552.
[5] Y. Nishihata, J. Mizuki, T. Akao, et al., Nature 418 (2002) 164–167.
[6] M. Cargnello, D.J.J. Jaén, G.J.C. Hernández, et al., Science 337 (2012) 713–717.
[7] A. Hellman, A. Resta, N.M. Martin, et al., J. Phys. Chem. Lett. 3 (2012) 678–682.
[8] N.M. Martin, M.V.D. Bossche, A. Hellman, et al., ACS Catal. 4 (2014) 3330–3334.
[9] F. Zhang, C. Hakanoglu, J.J.A. Hinojosa, et al., Surf. Sci. 617 (2013) 249–255.
[10] N. Dragos, T. George, N.M. David, et al., Nat. Chem. 5 (2013) 916–923.
[11] Y. Xiao, K. Xie, Angew. Chem. Int. Ed. 61 (2022) e202113079.
[12] J.H. Kim, J.K. Kim, J. Liu, et al., ACS Nano 15 (2021) 81–110.
[13] Y. Yang, S. Wang, X. Tu, et al., Exploration (2022) 20220060.
[14] A. Mussio, M. Danielis, N.R.J. Divins, et al., ACS Appl. Mater. Interfaces 13 (2021) 31614–36123.
[15] K. Persson, A. Ersson, K. Jansson, et al., J. Catal. 243 (2006) 14–24.
[16] S.A. Yashnik, Y.A. Chesaov, A.V. Ishchenko, et al., Appl. Catal. B 204 (2017) 89–106.
[17] E.D. Goodman, S. Dai, A.C. Yang, et al., ACS Catal. 7 (2017) 4372–4380.
[18] S.J. Cho, S.K. Kang, Catal. Today 93-95 (2004) 561–566.
[19] N. Sadokhina, G. Smedler, U. Nylén, M. Olofsson, et al., Appl. Catal. B 236 (2018) 384–395.
[20] A. Gremminger, P. Lott, M. Merts, et al., Appl. Catal. B 218 (2017) 833–843.
[21] P. Lott, M. Eck, D.E. Doronkin, et al., Appl. Catal. B 278 (2020) 119244.
[22] P. Qu, S. Wang, W. Hu, et al., Catal. Commun. 135 (2020) 105900.
[23] X. Li, L. Dai, Z. He, et al., Sens. Actuators B: Chem. 298 (2019) 126827.
[24] X. Mao, A.C. Foucher, T. Montini, et al., J. Am. Chem. Soc. 142 (2020) 10373–10382.
[25] C.S.A. Jesuina, F.O. Lais, C.O. Alcineia, et al., Int. J. Hydrog. Energy 44 (2019) 27329–27342.
[26] H. Chen, H. Shuang, W. Lin, et al., ACS Catal. 11 (2021) 6193–6199.
[27] Y. Ryou, J. Lee, S.J. Cho, et al., Appl. Catal. B 212 (2017) 140–149.
[28] Y. Yan, H. Li, H. Zhang, et al., Chin. Chem. Lett. 30 (2019) 1153–1156.
[29] T.P.O. Mkhwanazi, M.D. Farahani, A.S. Mahomed, et al., Appl. Catal. B 275 (2020) 119118.
[30] X. Chen, Y. Zheng, F. Huang, et al., ACS Catal. 8 (2018) 11016–11028.
[31] J. Xu, M. Zhong, N. Song, et al., Chin. Chem. Lett. 34 (2023) 107359.
[32] J. Chen, J. Zhong, Y. Wu, et al., ACS Catal. 10 (2020) 10339–10349.